H1prelim-12-041
March 2012

Submitted to

XX International Workshop on Deep-inelastic scattering and Related Subjects, DIS 2012
March 26-30, 2012, Bonn

Abstract: **109**
Parallel Session: **Structure functions**

Electronic Access: www-h1.desy.de/h1/www/publications/conf/conf_list.html

A Measurement of the HERA Luminosity using elastic QED Compton events detected by the H1 experiment

H1 Collaboration

Abstract

A precise knowledge of the integrated luminosity of the HERA collider is relevant for various types of cross section measurements and for a precise determination of the parton density functions of the proton. At ep colliders, the integrated luminosity is often measured in the Bethe Heitler process, using dedicated detectors located at small angles. In this paper, an alternative measurement of the integrated luminosity is presented, exploiting the elastic QED Compton process $ep- > e\gamma p$. Both the electron and the photon are detected in the H1 backward calorimeter. The integrated luminosity of the data recorded in 2003 to 2007 is determined with a relative precision of $\pm 0.85\%$(stat) $\pm$ 2.12%(sys), where (stat) is the statistical uncertainty and (sys) is the total systematic uncertainty. The measurement is found to be compatible with the corresponding Bethe-Heitler analysis.

1 Introduction

For particle collider experiments, knowledge of the integrated luminosity is an essential ingredient to any type of data analysis. For a particle collider with beam particles p_1 and p_2, the instantaneous luminosity is defined as

$$\mathcal{L}(t) = \frac{fnN_1N_2}{A} \tag{1}$$

where f is the revolution frequency, n is the number of colliding bunches per revolution, and N_1 (N_2) is the number of particles of type p_1 (p_2) per bunch. The effective cross section of the beams is A. The time-integrated luminosity relates the cross section $\sigma_{p_1p_2\rightarrow X}$ of a reaction $p_1p_2 \rightarrow X$ to the number of events expected $N_{p_1p_2\rightarrow X}$ in the time interval T

$$\int_T \mathcal{L}(t)dt = \frac{N_{p_1p_2\rightarrow X}}{\sigma_{p_1p_2\rightarrow X}}. \tag{2}$$

As it is difficult to determine all beam parameters at percent level, in particular those defining A, the integrated luminosity often is determined by counting the number of observed events in a specific reaction $p_1p_2 \rightarrow X$ with a well known cross section.

At HERA, the colliding beams are protons and electrons[1]. The proton beam energy is $E_p = 920\,\mathrm{GeV}$ and the electron beam energy is $E_0 = 27.6\,\mathrm{GeV}$. The reaction which is used to determine the luminosity is the production of an additional photon in elastic ep scattering, $ep \rightarrow e\gamma p$. Depending on the phase space considered, this process is referred to as Bethe-Heitler (BH) scattering or QED Compton (QEDC) scattering. In the BH process both the electron and the photon are emitted colinear to the incident electron. The corresponding cross section is very large, $\mathcal{O}(100\,\mathrm{mb})$. Dedicated small angle detectors are used to record BH events. In contrast, for QEDC scattering, the particles have a sizeable transverse momentum with respect to the incident electron. However, the momentum transfer at the proton vertex is still close to zero. At larger momentum transfer, inelastic processes dominate and the reaction becomes sensitive to the proton structure function [1]. Within the phase-space considered for this analysis, typical elastic QEDC cross sections are $\mathcal{O}(0.1\,\mathrm{nb})$. The events are recorded using the main detector also used for other physics analyses.

2 H1 Detector

A detailed description of the H1 detector can be found in [2]. Only the components essential to the present analysis are described here. The origin of the H1 coordinate system is the nominal ep interaction point. The direction of the proton beam defines the positive z–axis (forward direction). Transverse momenta are measured in the xy plane. Polar (θ) and azimuthal (φ) angles are measured with respect to this reference system. The pseudorapidity is defined as $\eta = -\log\tan(\theta/2)$.

[1] In this paper the term "electron" is used generically to refer to both electrons and positrons.

In the backward region $-4.0 < \eta < -1.4$, a lead-scintillating fibre calorimeter (SpaCal) [3] is used for the identification and measurement of both the scattered electron and the scattered photon. The energy resolution for electromagnetic showers is $\sigma(E)/E \simeq 7.1\%/\sqrt{E/\mathrm{GeV}} \oplus 1\%$. The electromagnetic section of the SpaCal is read out in cells of size 4×4 cm in the xy plane. The xy position of a shower is reconstructed as an energy weighted mean of the cell centres. After applying xy dependent corrections, the position resolution is of order 3.5 mm in the energy range relevant for this analysis.

The liquid argon (LAr) calorimeter covers the range $-1.5 < \eta < 3.4$. Its energy resolution is $\sigma(E)/E \simeq 50\%/\sqrt{E/\mathrm{GeV}}$ for hadronic showers, as obtained from test beam measurements [4].

The central region of the detector is equipped with a set of tracking detectors (CTD). There are the two concentric central jet chambers (CJC) and the central silicon tracker (CST) [5], which together measure the transverse momenta of charged particles in the angular range $20° < \theta < 160°$. In the backward region the tracking is complemented by the backward proportional chamber (BPC), located directly in front of the SpaCal. The central inner proportional chamber (CIP) [6] is located between the CJC and the CST. It consists of five chambers with a radial spacing of 9 mm, where the innermost layer is located at a radius of 15.7 cm. In φ there is a 16-fold segmentation, whereas in z the segments have variable size, ranging from 1.8 cm in the innermost layer to 2.3 cm in the outermost layer. The CIP has an angular acceptance in the range $10° < \theta < 170°$.

The calorimeters and tracking detectors are located inside a large superconducting solenoid, providing a uniform field of 1.16 T strength. The return yoke of the solenoid is instrumented and serves as a muon detector. Further away from the detector, at $z < -6$ m there is a system of scintillators (VETO). Timing signals from the VETO were used during data taking to reject particles originating from non-ep interactions of the proton beam in the HERA tunnel. The luminosity system for measuring the Bethe-Heitler process consists of an electron tagger located at $z = -5.4$ m and a photon calorimeter located at $z = -103$ m.

3 Signal and Background processes

Various Monte Carlo event generators (MC) are used to predict signal and background processes. A GEANT [7] simulation of the H1 detector is performed for each generated event, where also the relevant time-dependencies such as changes to the detector setup and varying beam conditions are taken into account. After detector simulation, the events are passed through the same reconstruction algorithms as were used on the data.

The QEDC signal is simulated using the COMPTON22 event generator [8]. This generator produces elastic, quasi-elastic and inelastic events. Only elastic QEDC events are taken as signal, the other events are treated as background. The fragmentation of quasi-elastic events is modelled using the SOPHIA package [9], whereas for inelastic events string fragmentation, implemented in PYTHIA [10] is used. For the elastic QEDC signal, final state radiation from the electron has been included in the COMPTON22 generator using the relevant PYTHIA routines.

Select exactly two SpaCal clusters	
Radial distance from beam $30 < R < 72\,\mathrm{cm}$	
Reconstruct CIP vertex	
Identify electron/photon	
One CIP vertex electron has CIP vertex photon has no CIP vertex	two CIP vertexes select hypothesis with $\Delta\varphi$ closest to $180°$
$\min(E_e, E_\gamma) > 7\,\mathrm{GeV}$ and $\max(E_e, E_\gamma) > 10\,\mathrm{GeV}$	
$\lvert z_{\mathrm{vtx}}\rvert < 35\,\mathrm{cm}$	
$170° < \Delta\varphi < 190°$	
$155.9° < \theta_e, \theta_\gamma < 169.5°$	
$\lvert\vec{P}_T^{\mathrm{miss}}\rvert < 0.3\,\mathrm{GeV}$	
No third SpaCal cluster with $R > 20\,\mathrm{cm}$ and $E > 2.2\,\mathrm{GeV}$	
Energy in LAr at $\theta < 10°$ is below $0.5\,\mathrm{GeV}$	
Only CTD track pointing to e or γ are allowed	

Table 1: Summary of the criteria to select QEDC events. Details are given in the text.

An important source of background are higher order QEDC processes, producing additional electron-positron pairs, $ep \to ep\, e^- e^+$. These processes are simulated using the GRAPE generator [11]. Other background originates mainly from various diffractive processes, namely deeply virtual Compton scattering (DVCS), Diffractive Vector Meson (VM) production and non-resonant diffraction. DVCS is modelled using the MILOU generator [12]. Diffractive Vector Meson (VM) production is simulated using the DIFFVM event generator [13], where the production of ρ, ω, ϕ, J/Ψ, Ψ' and Υ is considered. For the case of ρ production, DIFFVM is modified such that decays to $\pi^0\gamma$ and $\eta^0\gamma$ are included. Non-resonant diffraction is simulated using the RAPGAP event generator [14]. Background from non-diffractive deep-inelastic scattering (DIS) is simulated using DJANGO [15] and is found to be negligible.

4 Event selection

Elastic QEDC events are selected by requiring two compact clusters in the electromagnetic section of the SpaCal. A summary of the selection criteria is given in Table 4. The radial distance from the beam, R, of the clusters is restricted. The condition $R > 30\,\mathrm{cm}$ ensures that particles originating from the nominal interaction region are within the CIP acceptance, whereas the requirement $R < 72\,\mathrm{cm}$ ensures that the showers are well contained in the SpaCal.

Electron trajectories are reconstructed using also the CIP chambers. Hits in the CIP chamber are associated to the SpaCal cluster in φ and adjacent hits are merged to CIP clusters in φ and z. This merging is done separately for each layer. A straight line fit of the CIP clusters and the SpaCal cluster in the rz plane is performed, where outliers are rejected. The coordinate r is the radial distance from the z axis, where the azimuthal direction is taken from the SpaCal cluster. After outlier rejection, there are up to five accepted CIP clusters, corresponding to the five CIP layers. If there is only one accepted CIP cluster, it is discarded. Next, the centre-of-gravity of the CIP clusters in the rz plane is calculated. Finally, the CIP centre-of-gravity in rz , together with the SpaCal energy and the SpaCal position are used to reconstruct a helix trajectory in three dimensions, pointing back to the origin of the interaction. For determining this helix, the beam spot and beam tilt are also used[2]. The direction of bending in the magnetic field is chosen assuming that the particle charge is equal to the charge of the beam lepton. The algorithm finally returns the origin of the interaction (CIP vertex) and the momentum vector at the CIP vertex.

The electron and the photon are then identified, making use of the helix fit results. If there is no CIP vertex, the event is rejected. If there is only one cluster which has a CIP vertex, that cluster is taken as the electron and the other cluster is taken as the photon. The photon momentum vector is calculated from the photon cluster energy and a straight line trajectory pointing from the electron's CIP vertex to the photon cluster position. If both clusters have CIP vertexes, it is assumed that the photon has converted into an electron-positron pair while passing the material in front of the CIP detector. For the reconstruction, two hypothesis are checked in that case. First, one of the clusters is taken as the electron, and the photon momentum is calculated using the energy and position of the other cluster as described above. The difference in azimuth between the so determined electron and photon candidate momenta, $\Delta\varphi_1$, is determined. Next, the role of the electron and the photon are exchanged and again the difference in azimuth, $\Delta\varphi_2$, is calculated. Finally a decision is taken for either the first or the second hypothesis, whichever has a difference in azimuth[3] closer to 180°. For elastic QEDC events, the probability to misidentify the particles, as predicted by the simulation, is 0.3% (16%) if one (both) clusters have CIP vertexes.

Once the electron and photon have been identified, the z position of the electron CIP vertex, z_{vtx} is checked. Only events where $|z_{\text{vtx}}| < 35\,\text{cm}$ are considered for the analysis. Having reconstructed the two calibrated particle momenta, additional requirements are added: on the most energetic particle's energy $\max(E_e, E_\gamma) > 10\,\text{GeV}$, on the least energetic particle's energy $\min(E_e, E_\gamma) > 7\,\text{GeV}$, on the polar angles $155.9^\circ < \theta_e, \theta_\gamma < 169.5^\circ$, on the difference in azimuth $170^\circ < \Delta\varphi < 190^\circ$ and on the modulus of the transverse component of the vector sum of the particle momenta $|\vec{P}_T^{\text{miss}}| < 0.3\,\text{GeV}$.

In addition there are veto conditions on additional activity in the detector. Events are rejected if the energy in the forward part of the LAr calorimeter, with polar angle $\theta < 10^\circ$, exceeds $0.5\,\text{GeV}$ or if there are tracks reconstructed in the central tracker. For this track counting, only high quality tracks linked to a primary vertex are selected and tracks which are pointing to either the electron or the photon are excluded.

The total number of elastic QEDC candidate events is 14277. The energies and polar angles are shown in figure 1. Within uncertainties, the variables are described. Of particular interest is the $|\vec{P}_T^{\text{miss}}|$ distribution, figure 2, where the data are compared to the prediction and all background sources are indicated. The ratio of data to the prediction is shown in figure 3. The $|\vec{P}_T^{\text{miss}}|$

[2]The beam spot is defined as the average x and y position of interactions which take place at $z = 0$. The beam tilt is a slope correction for interactions at $z \neq 0$. These parameters were monitored during the H1 operation with the help of the CJC detector.

[3]The difference in azimuth is defined such that it is in the range $0^\circ \leq \Delta\varphi < 360^\circ$. Where necessary, multiples of 360° are added.

distribution is described within the uncertainties. The cut $|\vec{P}_T^{\text{miss}}| < 0.3\,\text{GeV}$ removes regions with large background contribuutions.

5 Systematic uncertainties

Systematic uncertainties on the elastic QEDC measurement may be categorised as follows: experimental uncertainties, background uncertainties and QEDC theory uncertainties. The experimental uncertainties originate from two sources, trigger and reconstruction. A summary of the systematic uncertainties is given in table 5. Additional time-dependent uncertainties may be

Trigger uncertainties	$\mathbf{0.22\%}$
Background uncertainties	$\mathbf{1.17\%}$
Reconstruction uncertainties	$\mathbf{1.41\%}$
QEDC theory uncertainties	$\mathbf{1.05\%}$
Statistical uncertainties	$\mathbf{0.85\%}$

Table 2: uncertainties on the determination of the luminosity using elastic QEDC events.

present in cases where the integrated luminosity determined in the present analysis is applied to different subsets of the H1 data.

5.1 Trigger uncertainties

During online data taking, events were selected based on a coincidence of certain trigger conditions. The main trigger condition was based on calorimetric information in the SpaCal. It had an efficiency of more than 95% for compact clusters with energies $E > 6\,\text{GeV}$, rising above 99.8% for energies $E > 10\,\text{GeV}$. Both the electron and the photon from the elastic QEDC reaction are efficient to fire the SpaCal trigger. For certain time periods there were small regions opposite in phi with reduced efficiency. This leads to an uncertainty of 0.02%. The other trigger conditions were related to the VETO detector. These trigger conditions had inefficiencies of typically 1% for data taken up to the year 2005 and 0.2% after 2006. They are corrected by applying time-dependent weights to the data events. The corresponding uncertainty is 0.22%.

5.2 Background uncertainties

The fraction of quasi-elastic and inelastic QEDC events predicted by the COMPTON22 generator have been verified by investigating the vector sum of the electron and photon transverse momenta, $\vec{P}_T^{\text{miss}}$. The vector $\vec{P}_T^{\text{miss}}$ is decomposed into components parallel to $(P_T^{||})$ and perpendicular to $(P_T^{\perp})$ the electron transverse momentum. Normalisation factors for the sum of quasi-elastic and inelastic QEDC, referred to as “non-elastic QEDC”, are extracted from fits to $P_T^{||}$ and $P_T^{\perp}$ for $|\vec{P}_T^{\text{miss}}| > 0.3\,\text{GeV}$. The distributions of $P_T^{||}$ and $P_T^{\perp}$ inside the analysis phase space as well as for $|\vec{P}_T^{\text{miss}}| > 0.3\,\text{GeV}$ are shown in figure 4. Both the parallel and the perpendicular components are described well. Outside the nominal analysis phase space the non-elastic QEDC contributions dominate at large $P_T^{\|}$ or large $P_T^{\perp}$. The normalisation factors determined in the fits are compatible with 1 within 25%.

The DVCS cross-section predictions obtained with the MILOU program are in agreement with recent H1 measurements [16]. Uncertainties of 20% for the elastic DVCS process and 50% for proton dissociative DVCS are considered.

The elastic VM production rates are normalised using dedicated selections as close as possible to the QEDC analysis. However, instead of requiring a photon in the SpaCal, a vector meson is reconstructed. The $\rho \to \pi^+\pi^-$, $\phi \to K^+K^-$, $J/\Psi \to \ell^+\ell^-$ ($\ell = e, \mu$) and $\Psi' \to \ell + \ell -$ are reconstructed from two oppositely charged tracks, detected in the CTD. The $\omega \to \pi^+\pi^-\pi^0$ is reconstructed from two charged tracks and one or two neutral calorimeter clusters. The $\Upsilon \to e^+e^-$ is reconstructed using a sample of photoproduction events, where an electron/positron pair from the Υ decay is reconstructed in the SpaCal, one of the SpaCal clusters matched with a central track, and the scattered electron is outside the acceptance of the H1 detector. The following normalisation uncertainties are considered: 20% on ρ and ϕ production, 50% on J/Ψ, and 100% on ω, Ψ' and Υ.

The rate of non-resonant diffractive events, simulated using RAPGAP, is normalised using a selection of low multiplicity final states, where the electron is reconstructed in the SpaCal and one up to to three additional particles are found. The uncertainty is found to be 30%.

For the QED Processes modelled by GRAPE, an uncertainty of 10% is estimated, taking into account possible higher order effects.

5.3 Reconstruction uncertainties

Reconstruction uncertainties originate mainly from the understanding of the SpaCal response to electrons and photons, when reconstructing their energy. The primary SpaCal energy calibration is done using electrons in DIS events [17]. However, the SpaCal energy response is slightly different for electrons and photons. Furthermore, it is found that the calibration can be improved by correcting the energy response as a function of the transverse cluster size, R_{log}. The variable R_{log} is calculated as a centre-of-gravity of SpaCal cell positions, using weights proportional to the logarithm of the energy. For the QEDC analysis, dedicated multiplicative calibration factors are applied to the SpaCal cluster energies for electrons, non-converted photons and converted photons, respectively. These multiplicative factors are taken to be a linear function of R_{log}. The corresponding constants are determined by applying double-angle calibration methods to a selection of QEDC events, where the cut on the momentum balance, $|\vec{P}_T^{\text{miss}}| < 0.3\,\text{GeV}$ is replaced by a loose cut on the difference in azimuth $170^\circ < \Delta\varphi < 190^\circ$. Fits are made to distributions of $P_T/P_{T,DA}$, where P_T is the measured transverse momentum and $P_{T,DA}$ is the predicted transverse momentum. The predicted transverse momentum is given by

$$P_{T,DA} = 2E_0 \left(\frac{1-\cos\theta_e}{\sin\theta_e} + \frac{1-\cos\theta_\gamma}{\sin\theta_\gamma} \right)^{-1}, \tag{3}$$

where θ_e and θ_γ are the polar angles of the electron and the photon, respectively. In addition to the calibration factors, calculated from fits of the position of the maximum in these distributions, the energy resolution is checked. The MC simulation has small deficits to describe tails towards lower transverse momenta in the $P_T/P_{T,DA}$ distributions for both electrons and photons. This is corrected for by applying an extra smearing of the reconstructed energies. An energy offset $\Delta E = (\delta - \tau)\, E_0/2$ is subtracted, where δ is a random number drawn from an exponential distribution. The parameter describing the expectation value of of the exponential is chosen as $\tau = 1\% \pm 0.5\%$. The difference $\delta - \tau$ is used for the smearing ΔE, such that the expectation value of ΔE is zero. This has the desired effect that the peak position of $P_T/P_{T,DA}$ is affected only little by the smearing. This procedure is applied for all generated electrons and photons which are matched to one of the reconstructed clusters. The τ parameters are varied independently for generated electrons and photons. Figure 5 shows the ratio $P_{T,e}/P_{T,DA}$ and $P_{T,\gamma}/P_{T,DA}$ for electrons and photons, respectively. The data agree with the simulation well within the systematic uncertainties. These are dominated by uncertainties of the energy resolution, described above, and by variations of the energy scale. The energy scale of the electrons and of the photons is varied by 0.5% each. In addition, a simultaneous variation of the electron and photon energy scale by another 0.5% is considered.

The SpaCal position resolution is found to be better in data than in the simulation. For this reason, the reconstructed position in MC is pulled towards the extrapolated SpaCal position of the corresponding generated particles. A constant $f = 0.14 \pm 0.05$ is used for this procedure, where $f = 0$ ($f = 1$) corresponded to the reconstructed (generated) position. The effect of the position resolution error is visible in figure 6, where the difference in azimuth, $\varphi_e - \varphi_\gamma$ is shown. The data are described by the prediction within the systematic uncertainties, which, for this figure, are dominated by the variation of f.

The CIP efficiency for electrons is determined in data and in the simulation using DIS events. It is found to be near 99% in data. For MC, the efficiency is near 99.5%. MC. A correction as a function of the SpaCal radius R is made by dropping a fraction of CIP vertexes in the simulation. The CIP spatial resolution is adjusted according to a comparison of the CIP vertex, reconstructed from the electron, and the CTD vertex, reconstructed from the $\pi^+\pi^-$ pair in elastic ρ decays. The conversion rate of photons in front of the CIP is underestimated in the simulation. In data, the conversion probability is around 32%, whereas the MC predicts 25%. This is corrected by mimicking conversion effects for a fraction of events with non-converted photons. For these events, extra CIP clusters near the expected position are added, and the energy response is scaled to match the expectation for converted photons. For estimating systematic effects, the three CIP related corrections described above are switched off one by one, and the difference is considered as uncertainty.

The alignment of the SpaCal and CIP detectors is found to be precise on the mm scale. Systematic effects are estimated by varying the SpaCal z position by ± 5 mm.

The distribution of the vertex at HERA is dominated by a Gaussian near $z = 0$ cm with a width of approximately 10 cm. The proton beam also exhibits prominent satellite peaks of similar width, leading to collisions near ± 70 cm. In addition, there is an excess of collisions near 40 cm, as compared to the simple model including only collisions from the main bunch and from the satellites. The simulated vertex distribution is reweighted such that the full interaction region is described, and the difference to the simple model is taken as systematic error.

The identification of compact electromagnetic clusters in the SpaCal is checked by relaxing selection cuts. The uncertainty is found to be 0.04%. The uncertainty on the CTD track reconstruction efficiency of 2% per track affects the analysis through the track veto. The efficiency of the LAr energy veto is checked by relaxing the veto condition to $E < 1\,\mathrm{GeV}$.

5.4 QEDC theory uncertainties

Uncertainties to the elastic QEDC cross section arise mainly from two sources: higher order corrections and the knowledge of the proton form factors.

In the original COMPTON22 generator, higher orders are simulated in the peaking approximation [18]. Improved higher order corrections have been calculated [19] in the leading logarithmic approximation using a photon radiator [20]. For the purpose of this analysis, the COMPTON22 events have event weights assigned such that the cross section predicted by the photon radiator method is reproduced. The difference to the original COMPTON22 prediction is taken as systematic error due to higher order effects. The elastic QEDC cross section also depends on the proton electric and magnetic form factors. In COMPTON22 a simple parameterisation (DIPOLE) of the form factors, based on a dipole model is implemented. For this analysis, recent form factor fits of DIS data [21] are taken into account, again using an event weighting technique. Two such parameterisations have been tested, with (TPE) and without (NOTPE) two-photon exchange corrections. As no two-photon exchange corrections are included in the COMPTON22 generator, the NOTPE parameterisation is preferred [22]. The difference between NOTPE and DIPOLE is taken as systematic uncertainty. It is worth noting that this difference is about a factor of two larger than the difference between NOTPE and TPE.

In figure 7 the distribution of the variable $(E - p_z)/(2E_0)$ is studied. This variable is calculated from the sum of the four-momenta of the electron and the photon. The distribution of this variable is expected to peak near 1. The tail to small $(E - p_z)/(2E_0)$ originates from initial state radiation, whereas values larger than 1 show up due to resolution effects. It is remarkable that the data are described within the systematic and statistical uncertainties for all values of $(E - p_z)/(2E_0)$. As expected, the peak region is dominated by experimental uncertainties, whereas the region of of small $(E - p_z)/(2E_0)$ is dominated by uncertainties of the QEDC cross section.

5.5 Time-dependent uncertainties

In order to apply the QEDC luminosity to other analyses, possibly using restricted H1 data sets, a luminosity calculation differential in time is required. This is achieved using DIS events measured in the SpaCal. The DIS selection follows the selection described in [17] but is restricted in phase space such that the rate is most insensitive to the average position of the interaction vertex in z. The DIS event counts for each run[4] are used to define the relative luminosity within one run, and the overall normalisation is taken from the QEDC analysis. The statistical uncertainty

[4] H1 data is grouped into runs, where new runs are started whenever data taking conditions changed. A run typically spans about 30 minutes of data.

of the DIS selection is negligible, but an additional time-dependent systematic error of 1.5% is introduced. It originates mainly from the SpaCal trigger and track linking efficiencies [17]. Figure 8 shows the results of the elastic QEDC analysis performed in bins of about $25\,\mathrm{pb}^{-1}$, normalised to the global QEDC analysis with the DIS yield corrections applied. Four data taking periods, corresponding to distinct configurations of the HERA machine or the H1 detector are indicated. During the periods (I) and (IV), the HERA machine was operated with a positron beam, whereas for (II) and (III) an electron beam was used. Furthermore, the H1 detector was modified slightly between the indicated periods. The two methods of measuring differential in time are in good agreement, taking into account the statistical fluctuations of the time-dependent QEDC analysis and the time-dependent systematic uncertainties of the DIS yield method.

6 Results

Elastic QED Compton events are selected in the H1 detector using the full data sample collected in the years 2003 to 2007. The luminosity of the data sample is determined by counting the data events and normalising the total MC prediction to the data. The statistical error amounts to 0.85%, whereas the total systematic error is 2.12%. For the selected data sample, the integrated luminosity is determined to be $\int \mathcal{L}(t)dt = 350.5 \pm 8.0\,\mathrm{pb}^{-1}$, in agreement with the Bethe Heitler measurement which has a relative uncertainty of 3.4%. A procedure to measure the luminosity of arbitrary data samples is defined based on time dependent corrections. These corrections are derived from an independent selection of DIS events an have a precision of 1.5%.

7 Summary

The integrated luminosity of the H1 data taken in the years 2003-2007 is determined using the QED Compton process. The precision of the measurement is 2.28%. The uncertainties are about equally shared between experimental uncertainties, understanding the elastic QEDC cross section and understanding the background to the measurement. The statistical uncertainty is small compared to the systematic uncertainties.

8 References

References

[1] A. Aktas *et al.* [H1 Collaboration], "Measurement of the proton structure function F2 at low Q**2 in QED Compton scattering at HERA," Phys. Lett. B **598** (2004) 159 [arXiv:hep-ex/0406029].

[2] I. Abt *et al.* [H1 Collaboration], "The H1 detector at HERA," Nucl. Instrum. Meth. A **386** (1997) 310;
I. Abt *et al.* [H1 Collaboration], "The Tracking, calorimeter and muon detectors of the H1 experiment at HERA"

[3] Nucl. Instrum. Meth. A **386** (1997) 348;
R. Appuhn *et al.* [H1 SPACAL Group], "The H1 lead/scintillating-fibre calorimeter," Nucl. Instrum. Meth. A **386** (1997) 397.

[4] B. Andrieu *et al.* [H1 Calorimeter Group], "Beam tests and calibration of the H1 liquid argon calorimeter with electrons," Nucl. Instrum. Meth. A **350** (1994) 57.
B. Andrieu *et al.* [H1 Calorimeter Group], "Results From Pion Calibration Runs For The H1 Liquid Argon Calorimeter And Comparisons With Simulations," Nucl. Instrum. Meth. A **336** (1993) 499.

[5] D. Pitzl *et al.*, Nucl. Instr. and Meth. A**454** (2000) 334 [hep-ex/0002044].

[6] J. Becker *et al.*, Nucl. Instrum. Meth. A **586** (2008) 190 [arXiv:physics/0701002].

[7] R. Brun *et al.*, CERN-DD/EE-84-1 (1987).

[8] A. Courau and P. Kessler, "QED Compton scattering in high-energy electron - proton collisions," Phys. Rev. D **46** (1992) 117,
V. Lendermann, Doctoral Thesis, University of Dortmund, 2002 [DESY-THESIS-02-004]

[9] A. Mucke, R. Engel, J. P. Rachen, R. J. Protheroe and T. Stanev, "Monte Carlo simulations of photohadronic processes in astrophysics," Comput. Phys. Commun. **124** (2000) 290 [arXiv:astro-ph/9903478].

[10] T. Sjostrand, P. Eden, C. Friberg, L. Lonnblad, G. Miu, S. Mrenna and E. Norrbin, "High-energy physics event generation with PYTHIA 6.1," Comput. Phys. Commun. **135**, 238 (2001) [arXiv:hep-ph/0010017].

[11] T. Abe, GRAPE-Dilepton version 1.1, "GRAPE-Dilepton (Version 1.1): A generator for dilepton production in ep collisions", Comput. Phys. Commun. **136** (2001) 126 [hep-ph/0012029].

[12] E. Perez, L. Schoeffel and L. Favart, "MILOU: A Monte-Carlo for deeply virtual Compton scattering", hep-ph/0411389.

[13] B. List, A. Mastroberardino, "DIFFVM: A Monte Carlo generator for diffractive processes in ep scattering" in A. Doyle *et al.* (eds.), Proceedings of the Workshop on Monte Carlo Generators for HERA Physics, DESY-PROC-1999-02 (1999) 396.

[14] RAPGAP 3.1: H. Jung, "Hard diffractive scattering in high-energy e p collisions and the Monte Carlo generator RAPGAP," Comput. Phys. Commun. **86** (1995) 147.

[15] G. Schüler and H. Spiesberger, Proc. of the Workshop on Physics at HERA, eds. W. Buchmüller, G. Ingelman, Hamburg, DESY (1992) 1419.

[16] F. D. Aaron *et al.* [H1 Collaboration], "Deeply Virtual Compton Scattering and its Beam Charge Asymmetry in $e^{\pm}p$ Collisions at HERA," Phys. Lett. B **681** (2009) 391 [arXiv:0907.5289 [hep-ex]].

[17] F. D. Aaron *et al.*, “Measurement of the Inclusive $e^{\pm}p$ Scattering Cross Section at High Inelasticity y and of the Structure Function FL,” Eur. Phys. J. C **71** (2011) 1579 [arXiv:1012.4355 [hep-ex]].

[18] E. Etim, G. Pancheri and B. Touschek, Nuovo Cim. **51B** (1967) 276;
G. Pancheri, Nuovo Cim. **60A** (1969) 321.

[19] H. Anlauf, H. D. Dahmen, P. Manakos, T. Mannel and T. Ohl [Darmstadt- Siegen Collaboration], “Higher order radiative corrections to the QED Compton events at HERA,” Z. Phys. C **52** (1991) 655.

[20] G. Montagna, O. Nicrosini and L. Trentadue, “QED radiative corrections to lepton scattering in the structure function formalism,” Nucl. Phys. B **357** (1991) 390.

[21] J. Arrington, W. Melnitchouk and J. A. Tjon, Phys. Rev. C **76**, 035205 (2007) [arXiv:0707.1861 [nucl-ex]].

[22] J. R. Arringtion, June 2011, private communication.

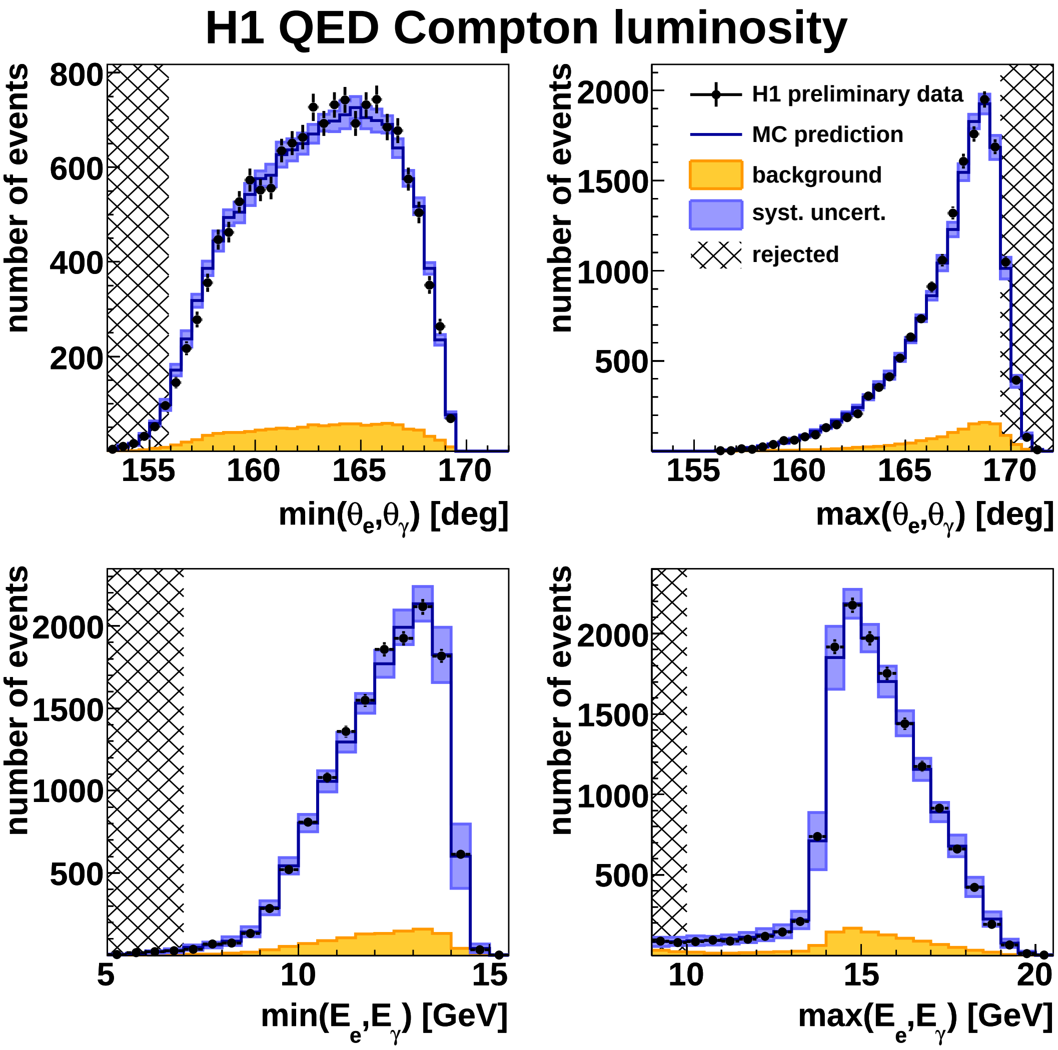

Figure 1: kinematic quantities of the selected electron/photon pair, (a) the minimum polar angle, (b) the maximum polar angle, (c) the minimum energy, (d) the maximum energy. The data are shown as black dots with the statistical uncertainties indicated as vertical bars. The prediction, normalized to the QEDC luminosity, is indicated as a solid line, with the systematic uncertainties attached as shaded area. Also shown is the contribution from background. The hatched areas are excluded by the selection criteria.

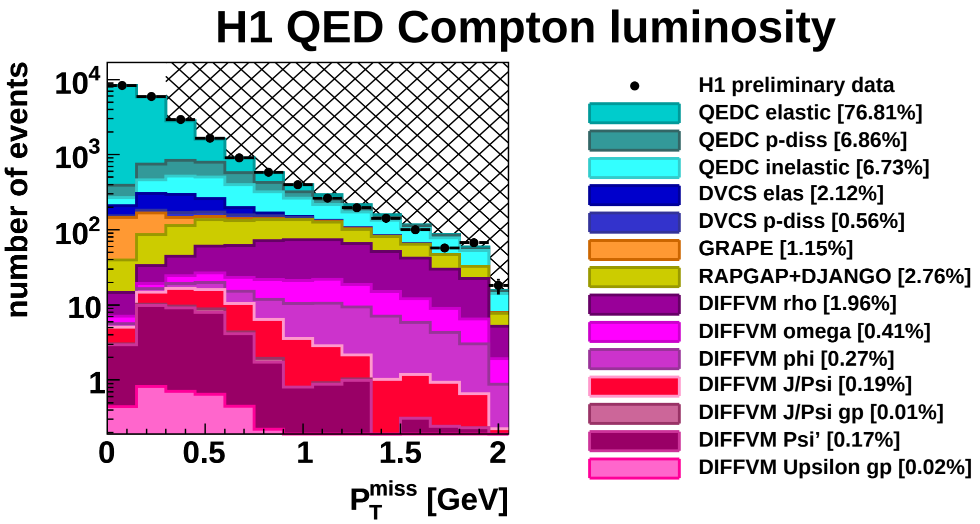

Figure 2: modulus of the vector sum of the electron and photon transverse momenta. The data are shown as black dots with the statistical uncertainties indicated as vertical bars. The prediction, normalized to the QEDC luminosity, is also shown, decomposed into contributions from the elastic QED Compton signal and the background sources considered for this analysis.

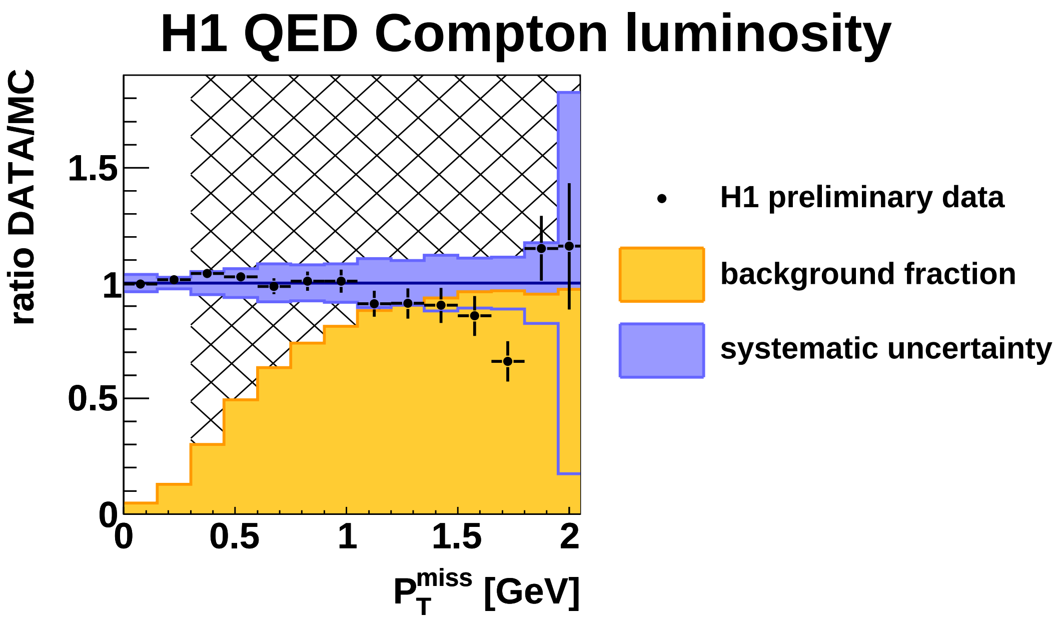

Figure 3: modulus of the vector sum of the electron and photon transverse momenta. The ratio of data to the prediction, normalized to the QEDC luminosity, is shown as black dots with the statistical uncertainties indicated as vertical bars. The background fraction and the size of the systematic uncertainties are also shown.

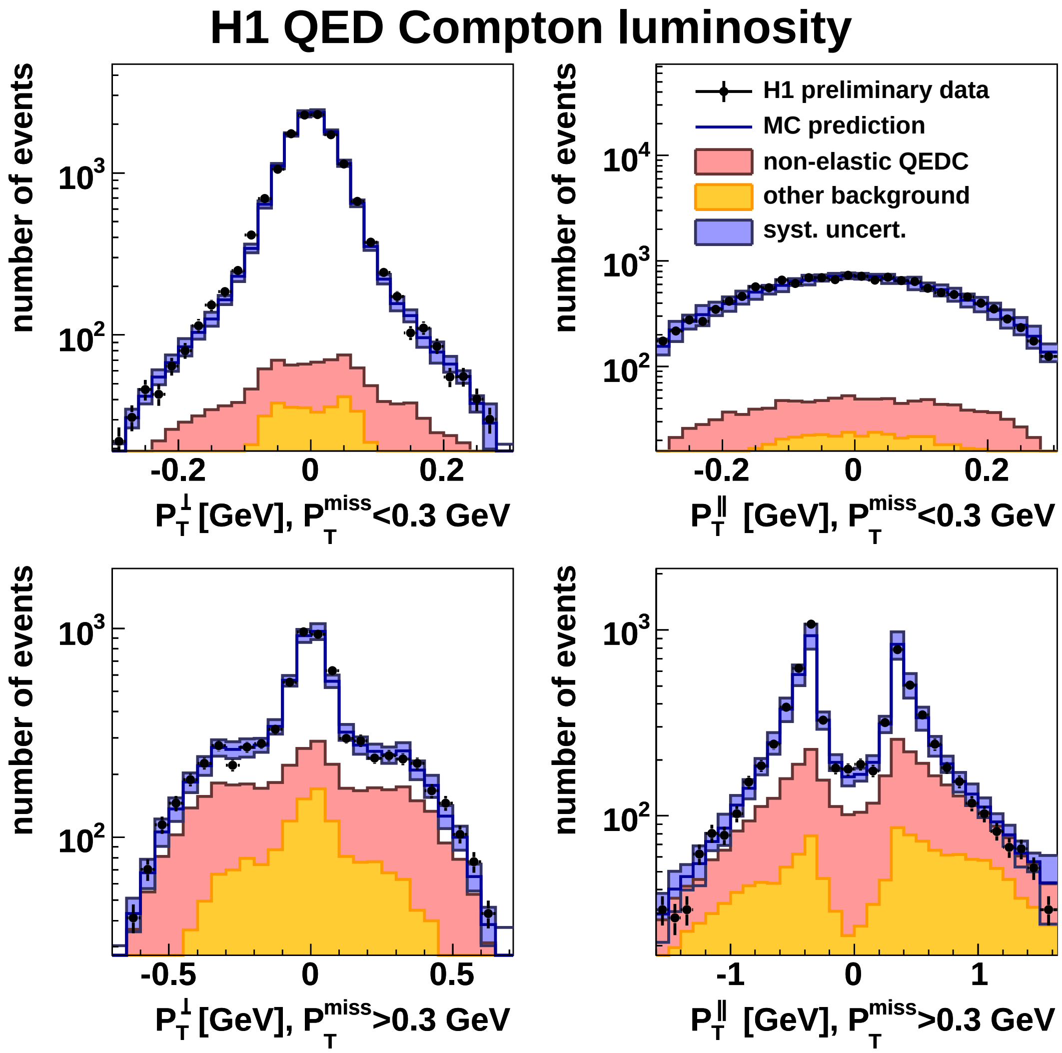

Figure 4: Components of the photon plus electron transverse momentum sum, $\vec{P}_T^{\text{miss}}$: left column the component perpendicular to the electron transverse moments, right column the component parallel to the electron transverse momentum. The upper row shows the distributions inside the analysis phase space, the lower row shows the distributions for $P_T^{\text{miss}} > 0.3\,\text{GeV}$. The data are shown as black dots with the statistical uncertainties indicated as vertical bars. The prediction, normalized to the QEDC luminosity, is indicated as a solid line, with the systematic uncertainties attached as shaded area. Also shown are the contribution from non-elastic QEDC and from other background sources.

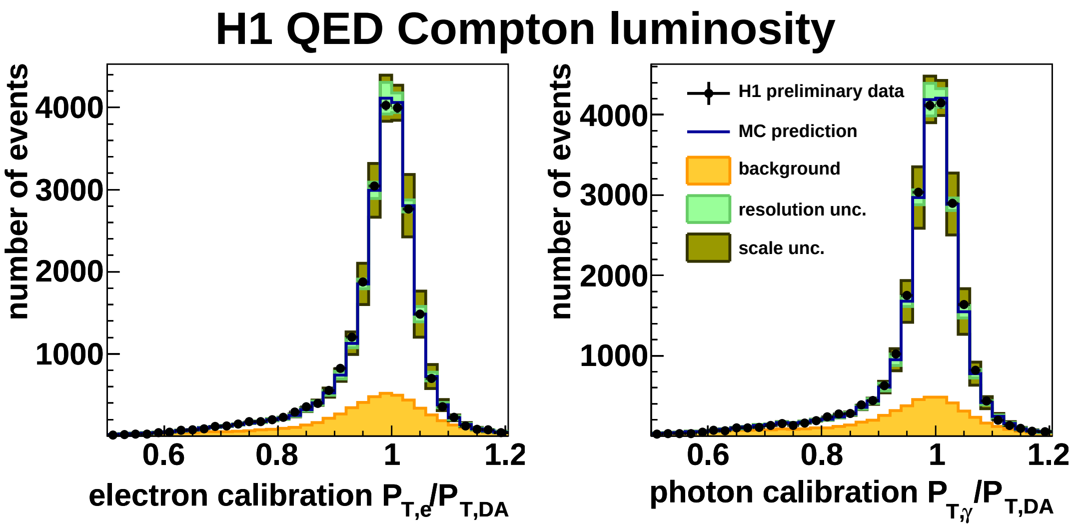

Figure 5: Ratio of measured to predicted transverse momentum for electrons and photons. The predicted transverse momentum $P_{T,DA}$ is calculated using the double angle method as explained in the text. The data are shown as black dots. The prediction, normalized to the QEDC luminosity, is shown as a solid line, with two types of systematic uncertainty attached. The inner (outer) uncertainty originates from the energy resolution (energy scale) variation. Energy scale variations common to the electron and photon are not included. Also shown is the contribution from background processes.

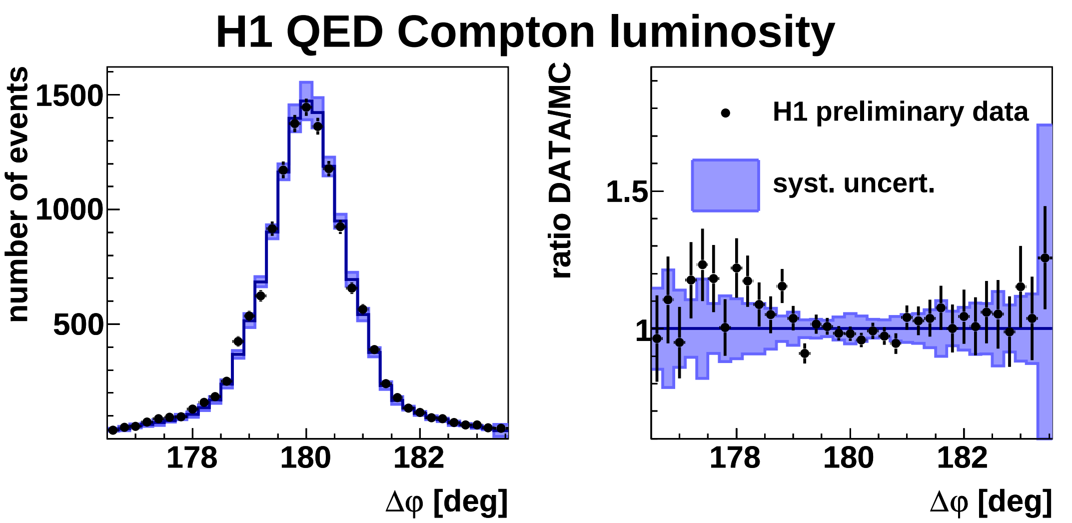

Figure 6: Difference in azimuth between the electron and the photon. On the left, the event counts are shown, whereas on the right the ratio of data to expectation is drawn. The data are shown as black dots with statistical uncertainties indicated as vertical bars. The prediction, normalized to the QEDC luminosity is shown as a solid line with systematic uncertainties attached as a shaded area.

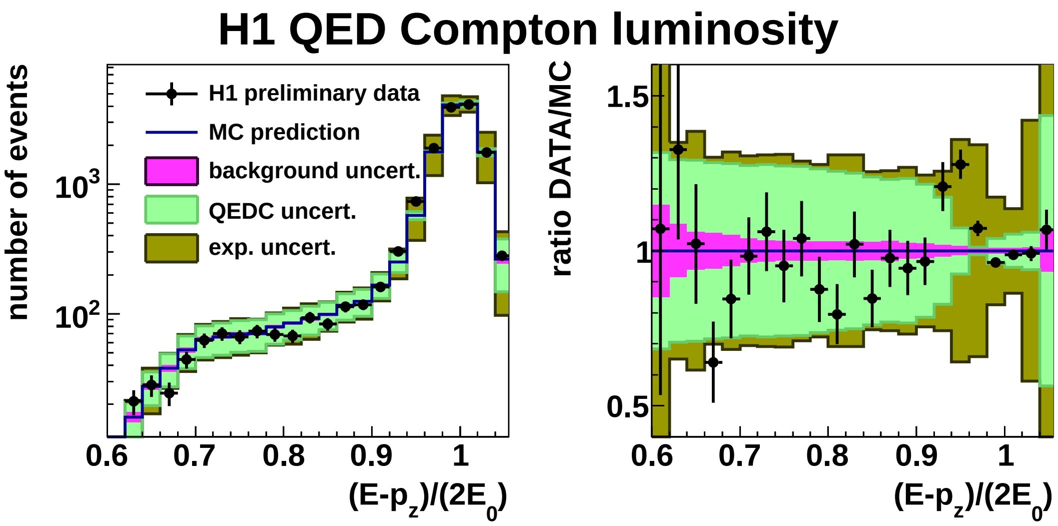

Figure 7: The variable $E-p_z$ calculated from the sum of the electron and photon four-momenta. On the left the event counts are shown, whereas on the right the ratio of data to expectation is drawn. The data are shown as black dots with the statistical uncertainties indicated as vertical bars. The prediction, normalized to the QEDC luminosity, is indicated as a solid line, with various components of the systematic uncertainties attached as shaded areas.

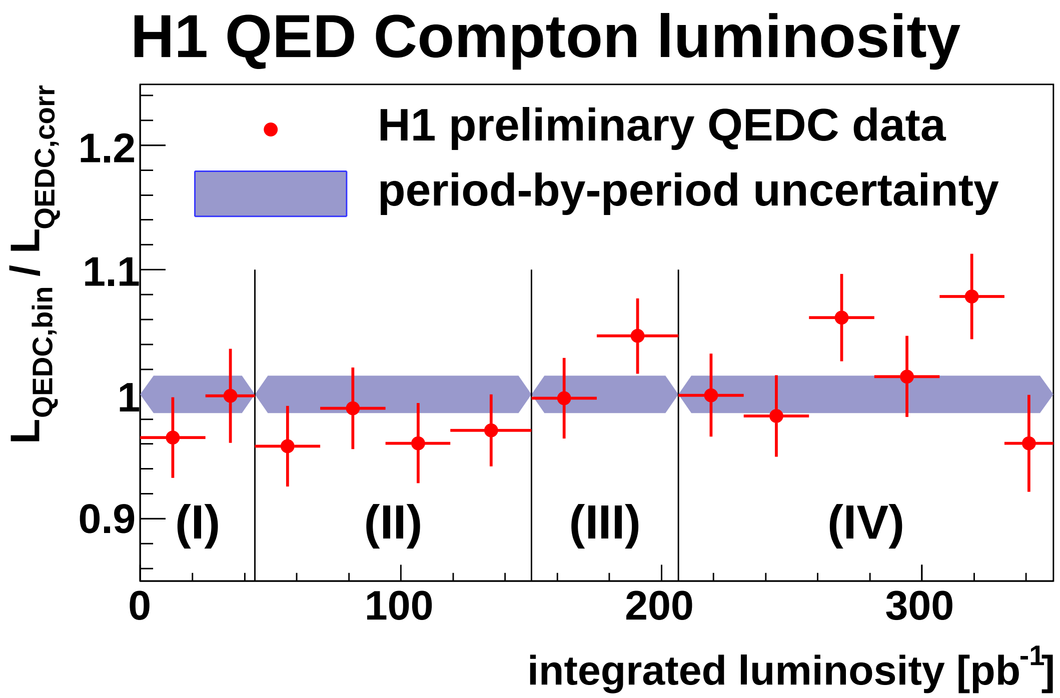

Figure 8: Integrated luminosity measured from elastic QEDC events in bins of approximately $25\,\mathrm{pb}^{-1}$, divided by the luminosity derived from the QEDC analysis on the full sample with time-dependent corrections applied. The statistical uncertainties of the binned QEDC analysis as well as the uncertaintes of the time-dependent corrections, here applied to four data taking periods (I)–(IV), are indicated.